

Numerical and Experimental Analysis of the Daughter Distribution in Liquid-Liquid Stirred Tanks

*Original*

Numerical and Experimental Analysis of the Daughter Distribution in Liquid-Liquid Stirred Tanks / Maluta, F.; Buffo, A.; Marchisio, D.; Montante, G.; Paglianti, A.; Vanni, M.. - In: CHEMICAL ENGINEERING & TECHNOLOGY. - ISSN 0930-7516. - STAMPA. - 44:11(2021), pp. 1994-2001. [10.1002/ceat.202100237]

*Availability:*

This version is available at: 11583/2978926 since: 2023-05-30T09:21:59Z

*Publisher:*

John Wiley and Sons

*Published*

DOI:10.1002/ceat.202100237

*Terms of use:*

This article is made available under terms and conditions as specified in the corresponding bibliographic description in the repository

*Publisher copyright*

(Article begins on next page)

Francesco Maluta<sup>1,\*</sup>  
Antonio Buffo<sup>2</sup>  
Daniele Marchisio<sup>2</sup>  
Giuseppina Montante<sup>1</sup>  
Alessandro Paglianti<sup>3</sup>  
Marco Vanni<sup>2</sup>

# Numerical and Experimental Analysis of the Daughter Distribution in Liquid-Liquid Stirred Tanks

The drop size distributions (DSDs) of a dilute immiscible liquid-liquid mixture were measured in a fully turbulent stirred tank operating at different impeller speeds. The results were used to infer the best daughter distribution function (DDF) leading to the best reproduction of the shape of the DSD. Bell-shaped, U-shaped, M-shaped, and uniform statistical DDFs were studied, producing from two to four daughters from each breakup event. A simplified approach from the literature was adopted to solve the population balance equation that considers the spectrum of the turbulence inside the tank obtained from computational fluid dynamics simulations. The U-shaped distribution producing four fragments better reproduces the shape of the experimental DSD in the studied system.



This is an open access article under the terms of the Creative Commons Attribution License, which permits use, distribution and reproduction in any medium, provided the original work is properly cited.

**Keywords:** Daughter distribution functions, Drop size distributions, Immiscible liquid-liquid mixtures, Population balance, Stirred tanks

*Received:* May 28, 2021; *revised:* July 21, 2021; *accepted:* August 24, 2021

**DOI:** 10.1002/ceat.202100237

## 1 Introduction

Liquid-liquid stirred tanks are very common in the oil and gas, pharmaceutical, food, and process industries. In recent years, the scientific community has shown how the design and scale-up of these systems can be carried out using mathematical modeling tools, based on computational fluid dynamics (CFD) and population balance modeling (PBM) [1–3]. The most complex part of these models is the description of the interaction between the eddies and the droplets, which can lead to droplet coalescence or breakage. Numerous models have been developed that try to describe these phenomena, and for in-depth reviews, the reader can refer to previous works [4–7].

In this work, the focus is on a very specific aspect of these models that has never been treated in depth, namely, the effect of the different daughter distribution functions (DDFs) on the model predictions. The daughter size distribution function expresses, in a mathematical form, the dimensional distribution of the droplets that are generated following the breakage of a mother droplet. Since the modeling approach based on the population balance describes the droplet population as an ensemble, discontinuous events such as breakage are treated by associating them with a probability due to their intrinsic chaotic nature. The daughter size distribution predicts the most probable droplet sizes following a breakage event. Attempts for obtaining this information from real or numerical experiments have been described in the literature [8–13], but despite the best efforts, the procedure is very complex and time consuming. The main reason for such difficulties stems from the number of breakup events to be detected to reach statistical significance for every initial mother size and fluid dynamic

condition, since by varying these two factors the breakage event may lead to very different outcomes.

Considering the complexity of the phenomenon, two main modeling approaches are adopted in the literature: a phenomenological approach, in which the DDF is derived from an approximated description of the fluid dynamics of the breakage event, and a statistical approach, in which the DDF has the form of a mathematical distribution function that does not vary depending on the fluid dynamics conditions or the initial dimension of the mother droplet. Due to the aforementioned limitations in the experimental validation of these modeling approaches, the statistical approach is often more popular due to its simplicity and ease of implementation, especially in case of CFD-PBM simulations. For this approach, at least three different types of shape for the DDF have been proposed: bell shape [14], U-shape [15] and M-shape [16], but no general consensus has been reached on these because the arguments used to justify the usage are often partial and contradictory.

<sup>1</sup>Dr. Francesco Maluta, Prof. Giuseppina Montante  
francesco.maluta@unibo.it  
Università di Bologna, Department of Industrial Chemistry "Toso Montanari", Viale Risorgimento 4, 40136 Bologna, Italy.

<sup>2</sup>Dr. Antonio Buffo, Prof. Daniele Marchisio, Prof. Marco Vanni  
Politecnico di Torino, Department of Applied Science and Technology, Corso Duca degli Abruzzi 24, 10129 Torino, Italy.

<sup>3</sup>Prof. Alessandro Paglianti  
Università di Bologna, Department of Civil, Chemical, Environmental and Materials Engineering, Via Terracini 28, 40131 Bologna, Italy.

In this work, we tried to infer which could be the most appropriate form of DDF and the average number of fragments generated by the breakup event, through comparing the numerical results of a model based on CFD and PBM with the experimental data measured in a laboratory-scale liquid-liquid stirred tank. Although other aspects of the model, such as the description of the coalescence and breakage frequencies and the fluid dynamics model play an essential role in the prediction of the drop size distribution (DSD), we still find it interesting to show how the DSD changes as only the DDF and the number of generated fragments vary. Although we are aware that the results obtained in this work may lack general validity due to the empirical nature of the investigation approach, the conclusions of this analysis are in line with some experimental observations of single-droplet breakage [8, 12, 13] and may therefore be useful to modelers and users.

## 2 Experimental Campaign

The system studied in this work was a stirred tank previously employed in liquid-liquid investigations [17, 18]; it consists of a cylindrical, flat-bottom, fully baffled tank with both its diameter  $T^{(1)}$  and its height equal to 0.23 m. The agitation was provided by a Rushton turbine with a diameter equal to  $T/3$ , mounted on a central shaft with an off-bottom clearance equal to  $T/2$ . The total volume of the mixture was equal to 9.8 L.

The liquid-liquid mixture consisted of commercial diesel fuel in demineralized water. The fluid densities were  $\rho_D = 810 \text{ kg m}^{-3}$  and  $\rho_C = 998 \text{ kg m}^{-3}$ , for the diesel fuel and water, respectively, while their viscosities were  $\mu_D = 3.5 \times 10^{-3} \text{ Pa s}$  and  $\mu_C = 10^{-3} \text{ Pa s}$ , respectively. The surface tension measured at room temperature was  $\sigma = 27.6 \text{ mN m}^{-1}$ .

Four different operating conditions were studied, corresponding to the impeller rotational speeds  $N$  of 500, 600, 700, and 800 rpm. Water was stirred for several minutes to reach the steady state and, subsequently, 9.7 mL of diesel fuel was injected close to the impeller, resulting in a diesel fuel volume fraction of  $10^{-3}$ .

A Spraytec laser diffraction system (Malvern Panalytical) equipped with a wet sample dispersion unit was employed to measure the drop size distribution. The light scattered as a laser beam passed through the liquid-liquid dispersion was collected, and the intensity was measured, by the instrument by means of several detectors covering a wide range of angles. The scattering pattern was then used to reconstruct the size distribution of the droplets in the sample. A 100-mL mixture sample was withdrawn from the vessel midway between two consecutive baffles at 40 min after the diesel fuel injection, to make sure that the system was at steady state. The sample was continuously recirculated by means of a small impeller through an optically accessible measurement cell positioned between the Spraytec transmitter and the receiver units. The influence of this impeller on the DSD was assessed and an optimal rotational speed of 2500 rpm was selected. The sample measurement time lasted for around 30 s, with a 10-s window average of the scattering pattern to allow the totality of the sample to pass through the measuring cell. The scattering pattern was used to obtain a discretized DSD in terms of the weighted volume

fractions of diesel fuel in the  $i$ th size bin with respect to the total dispersed-phase volume in the sample. In the present measurements, multiple scattering does not influence the accuracy of the results since the detected obscuration was significantly lower than the critical value above which multiple scattering must be considered.

The average DSD values obtained from triplicate measurements in the laser granulometry analysis are shown in Fig. 1, together with error bars denoting the standard deviation for each diameter class.

The volumetric distributions show two distinct peaks, a lower one shifted towards smaller diameters and a higher one shifted towards larger diameters. The measured Sauter mean diameters in the different conditions are equal to  $47.6 \mu\text{m}$  for  $N = 500 \text{ rpm}$ ,  $35.7 \mu\text{m}$  for  $N = 600 \text{ rpm}$ ,  $32.1 \mu\text{m}$  for  $N = 700 \text{ rpm}$ , and  $25.7 \mu\text{m}$  for  $N = 800 \text{ rpm}$ .

## 3 Numerical Simulations

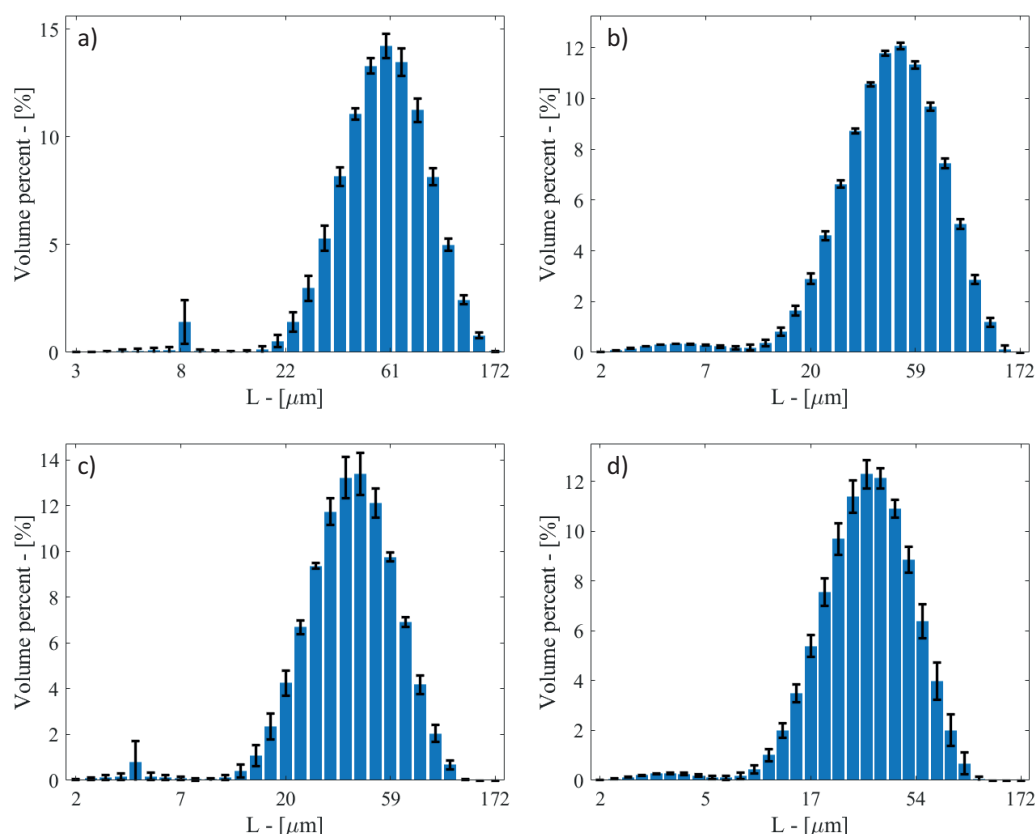
A simplified zero-spatial dimensional model was adopted to describe the evolution of the DSD in the operating conditions presented in Sect. 2, just considering the volume distribution of the turbulent dissipation rate  $\varepsilon$ . To obtain the distribution of  $\varepsilon$ , single-phase Reynolds-averaged Navier-Stokes (RANS) CFD simulations were performed in OpenFOAM 5.0 with a high-quality mesh and a modeling approach that produced grid-independent turbulent flow fields in good agreement with experimental data [18]. The model is based on the Eulerian description of both liquid phases, the two-fluid model, and the turbulence closure was achieved by means of the standard  $k$ - $\varepsilon$  turbulence model [18]. Successively, a probability density function,  $g(\varepsilon)$ , for each operating condition was built as:

$$g(\varepsilon) = \frac{1}{V} \frac{dv(\varepsilon)}{d\varepsilon} \quad (1)$$

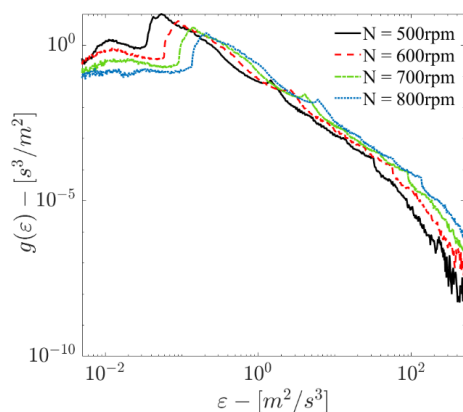
with  $v(\varepsilon)$  being the computational cells volume with a turbulent dissipation rate in the interval  $\varepsilon, \varepsilon + d\varepsilon$ , and with  $V$  being the total volume of the tank. The volumetric distributions of  $\varepsilon$  for the four conditions studied in this work are shown in Fig. 2.

Fig. 2 shows that the volume distribution of  $\varepsilon$  is shifted towards higher values as the impeller rotational speed increases and that the shape of the distribution is preserved, as expected since the tank is in a fully turbulent regime for all four cases analyzed in this work. The volume average  $\varepsilon$  is equal to 0.75, 1.31, 2.08, and  $3.10 \text{ m}^2 \text{ s}^{-3}$  for the four simulations obtained at impeller rotational speeds from 500 to 800 rpm, respectively.

As previously done by Buffo et al. [19], the spatial distribution of  $\varepsilon$  was used to calculate the breakage rate, which in the present work was modeled with the kernel developed by Alopaeus et al. [14]. The kernel was modified with the adoption of a scalar correction to account for the grid dependence of the parameters, as was done in a previous study [18], and the resulting breakage ( $h$ ) kernel is reported in Eq. (2).



**Figure 1.** Average experimental DSDs obtained at (a) 500 rpm, (b) 600 rpm, (c) 700 rpm, and (d) 800 rpm. Error bars represent the standard deviation for each class.



**Figure 2.** Volume distribution of the turbulent dissipation rate in the tank at the steady state for different impeller rotational speeds.

$$h(L_j) = C_1^0 (\epsilon F)^{\frac{1}{3}} \operatorname{erfc} \left( \sqrt{C_2^0 \frac{\sigma}{\rho_C (\epsilon F)^{\frac{2}{3}} L_j^3} + C_3^0 \frac{\mu_D}{\sqrt{\rho_C \rho_D} (\epsilon F)^{\frac{1}{3}} L_j^{\frac{4}{3}}}} \right) \quad (2)$$

where the values of the grid-independent parameters in the breakup kernel,  $C_1^0 = 2.98$ ,  $C_2^0 = 0.12$ , and  $C_3^0 = 0.25$ , were taken

from a previous investigation [18], and the scalar correction  $F$  results from the ratio of the presumed turbulent dissipation rate in the impeller zone predicted with an infinitely fine mesh and the turbulent dissipation rate predicted with the adopted computational grid, and it is equal to 1.17 in this work [18]. In the very dilute conditions considered in this work, one common assumption is to neglect the coalescence inside the stirred tank [20]. Thus, the resulting population balance equation (PBE) solved in this work is:

$$\frac{\partial n(L)}{\partial t} = \int_L^\infty \beta(L, \ell) h(\ell) n(\ell) d\ell - h(L) n(L) \quad (3)$$

where  $n(L)$  is the DSD and  $\beta$  is the DDF.

Different statistical DDFs corresponding to different shapes were adopted to describe the fragment generation, and they are reported in the following in terms of size-based distributions. The DDF by Laakkonen et al. [21] models the breakage event as a beta distribution, resulting in a bell shape, in which symmetric breakup is considered as the event with the highest probability, and for a generic number of fragments,  $p$ , it reads:

$$\beta(L_i, L_j) = p^3 \frac{L_i^2}{L_j^3} \left( 3 + \frac{11}{2} C_4 + 3 C_4^2 + \frac{1}{2} C_4^3 \right) \left( \frac{L_i^3}{L_j^3} \right)^2 \left( 1 - \frac{L_i^3}{L_j^3} \right)^{C_4} \quad (4)$$

where  $L_i$  and  $L_j$  are the daughter drop size and mother drop size, respectively,  $C_4$  is a parameter related to the number of fragments as  $p = \left(\frac{4}{3} + \frac{C_4}{3}\right)$ , and therefore, it assumes the value of 2 for a binary, 5 for a ternary, and 8 for a quaternary breakage.

The DDF by Diemer and Olson [22] is a generalized form of the distributions of Hill and Ng [23] and it can assume different shapes depending on the value of the parameter  $q$ . In this work, just two values of  $q$  were studied, namely,  $q = 0.5$  which gives a U-shaped DDF and  $q = 1$  which gives a uniform daughter distribution. The DDF expression reads:

$$\beta(L_i, L_j) = p^3 \frac{L_i^2}{L_j^3} \left( \frac{\Gamma(qp)}{\Gamma(q)\Gamma(q(p-1))} \right) \left( \frac{L_i^3}{L_j^3} \right)^{q-1} \left( 1 - \frac{L_i^3}{L_j^3} \right)^{q(p-1)-1} \quad (5)$$

where  $\Gamma$  denotes the gamma function.

The last DDF studied in this work is a logistic-normal distribution that, for values of the parameter  $r$  between 1.5 and 2.2, assumes an M-shape. In this work,  $r$  was taken as equal to 2, and the expression for this distribution is given in Eq. (6):

$$\beta(L_i, L_j) = p^3 \frac{L_i^2}{L_j^3} \left( r \sqrt{\pi} \frac{L_i^3}{L_j^3} \left( 1 - \frac{L_i^3}{L_j^3} \right) \right)^{-1} \exp \left( - \left( \log \left( \frac{L_i^3/L_j^3}{1 - L_i^3/L_j^3} \right) \right)^2 / 2r^2 \right) \quad (6)$$

It is worth remarking that, for every DDF, the following relationships must hold:

$$p = \int_0^{L_j} \beta(\ell, L_j) d\ell \quad (7)$$

$$L_j^3 = \int_0^{L_j} \ell^3 \beta(\ell, L_j) d\ell \quad (8)$$

To check if the DDF can be used, these two definite integrals must be evaluated. Eq. (7) expresses the condition that the moment of order zero of the DDF must be equal to the number of fragments, while Eq. (8) forces the third-order moment of DDF to be equal to the volume of the mother droplet. When such relationships are not valid, the results obtained may suffer mass imbalances. For this reason, the M-shaped logistic-normal distribution was only used in this work by considering  $p = 2$ , since an analytical solution of the integral of the moments of this statistical DDF does not exist.

The PBE was solved with the quadrature-based method of moments (QMOM) with six quadrature nodes, with the same procedure as presented by Buffo et al. [19]. A log-normal distribution with a mean diameter equal to 1 mm and a standard deviation equal to 0.15 mm was assumed as the initial DSD. The differential equation was solved in MATLAB R2019b with the Adams-Bashforth-Moulton variable-step, variable-order solver of orders 1 to 13, ode113, with absolute and relative

error tolerances of  $10^{-8}$ . The PBE final resolution time was determined from a time sensitivity study performed for each condition, and steady state was assumed once the evolution of the moments reached a plateau. The volume-averaged kernels were calculated with the trapezoidal numerical integration method. The DDFs were integrated with the adaptive quadrature algorithm with an absolute error tolerance of  $10^{-8}$  and the validity of Eqs. (7) and (8) was ensured.

By using the QMOM for the solution of the PBE, the information regarding the shape of the DSD is lost since only its moments are evaluated. This is a well-known limitation of the QMOM, with respect to other methods, such as classes or Monte-Carlo methods, which are better suited for predicting the shape of the distribution but, in turn, are more computationally expensive. However, some techniques to reconstruct the shape of a distribution from its moments are available [24]. As commonly done in the literature [25, 26], the extended QMOM (EQMOM) with a log-normal distribution as a kernel density function was used to obtain the DSD from the moment set available from the numerical solution [1], thus assuming a sum of two log-normal distributions with the same variance. The DSD was successively discretized in the same bins as the experimental DSD, for a better comparison.

## 4 Results and Discussion

Several simulations were run changing the shape of the DDF and the number of fragments. Namely, the beta distribution, Eq. (4), with two, three, and four daughters, the U-shaped DDF, Eq. (5), with two, three, and four daughters, the uniform distribution, Eq. (5), with two and three daughters, and the M-shaped distribution, Eq. (6), with two daughters were studied, resulting in nine different simulations. The resulting moments of order  $k$  from 1 to 5 were divided by the 0th order moment,  $M_{k,0}$ , and their percent deviations,  $\Delta k_0$ , from the corresponding experimental moment ratio were calculated as:

$$\Delta k_0 = \left| \frac{M_{k,0}^{\text{Num}}}{M_{k,0}^{\text{Exp}}} - 1 \right| \times 100 \quad (9)$$

where the superscripts Num and Exp indicate the moments from the numerical simulations and the experiments, respectively. In this way the numerical results and the experimental data are compared consistently, meaning that, the lower the deviation for all the first five-order moments, the better is the agreement between the predicted DSD and the experimental one. It is also worth remarking that a similar comparison is uncommon in the literature, since more often only the numerical and experimental Sauter mean diameters (i.e., the ratio between the third-order moment and the second-order moment with respect to the droplet size) are compared, especially when surface phenomena are of interest. Such an analysis reveals that all the DDF studied in this work predict a Sauter mean diameter in general agreement with the experimental one, as reported in Tab. 1, with the maximum deviation from the experimental data equal to 30.0 % obtained with a beta distribution with four daughters at 500 rpm, and an overall average deviation of 13.6 %. Thus, when just the Sauter mean diameter is of interest,

the choice of the DDF does not substantially affect the predictions.

It is worth mentioning that the kernel parameters were obtained for a binary breakage and therefore the Sauter mean diameters obtained with  $p = 2$  are in better agreement with the experiments. In the present study, changing the kernel parameters shifts the distribution but it does not change the shape of the DSD.

The analysis of the deviations from the experimental moment ratio allows the identification of the DDF that better describes the shape of the experimental distribution. The deviations for each moment ratio, for each DDF and number of daughters in all the operating conditions considered in this work are reported in Fig. 3.

Fig. 3 shows that increasing the number of daughters reduces the percent deviation  $\Delta k_0$  and that the deviations of the lower-order moments ratio are generally higher than the deviations of the higher-order moments ratio. The DDF that exhibits the lowest deviation from the experiments in all the operating conditions is the U-shaped DDF with the formation of four daughter droplets. This finding is consistent with previous experimental observations [8, 12, 13], in which the most-observed outcome of a breakage event for a liquid droplet is the formation of two large droplets and a limited number of smaller satellite drops. The corresponding DSDs are compared against the experimental DSDs in Fig. 4.

The numerical simulations that produced the DSD of Fig. 4 predict two distinct peaks as observed in the experimental volumetric distributions. Both peaks show higher volume fractions than the experimental peaks, since the numerical DSD are less dispersed than the experimental ones. This behavior

**Table 1.** Sauter mean diameters as obtained from the experiments and from the simulations with different DDFs at different impeller rotational speeds.

	Sauter mean diameter [ $\mu\text{m}$ ] at			
	500 rpm	600 rpm	700 rpm	800 rpm
Experimental	47.6	35.7	32.1	25.7
$\beta$ , two daughters	41.3	34.5	29.7	26.0
$\beta$ , three daughters	36.1	30.2	26.0	22.8
$\beta$ , four daughters	33.3	28.0	24.0	21.0
U, two daughters	41.8	35.0	30.1	26.5
U, three daughters	36.6	30.7	26.4	23.2
U, four daughters	34.0	28.5	24.5	21.5
Uniform, two daughters	41.1	34.4	29.6	26.0
Uniform, three daughters	36.0	30.2	26.0	22.8
M, two daughters	41.1	34.3	29.5	25.9

may be due to the choice of the log-normal distribution as kernel density function for the reconstruction of the distribution from the moments. Moreover, the lower numerical peaks are shifted towards larger diameters, with respect to the corresponding experimental peaks, and conversely the higher numerical peaks are shifted towards smaller diameters with respect to the corresponding experimental ones. The numerical simulations with the U-shaped DDF predict the overall shape of the experimental DSDs but cannot fully reproduce their extents.

The shape of the predicted DSD changes when different DDFs are used. By means of example, in Fig. 5, the numerical

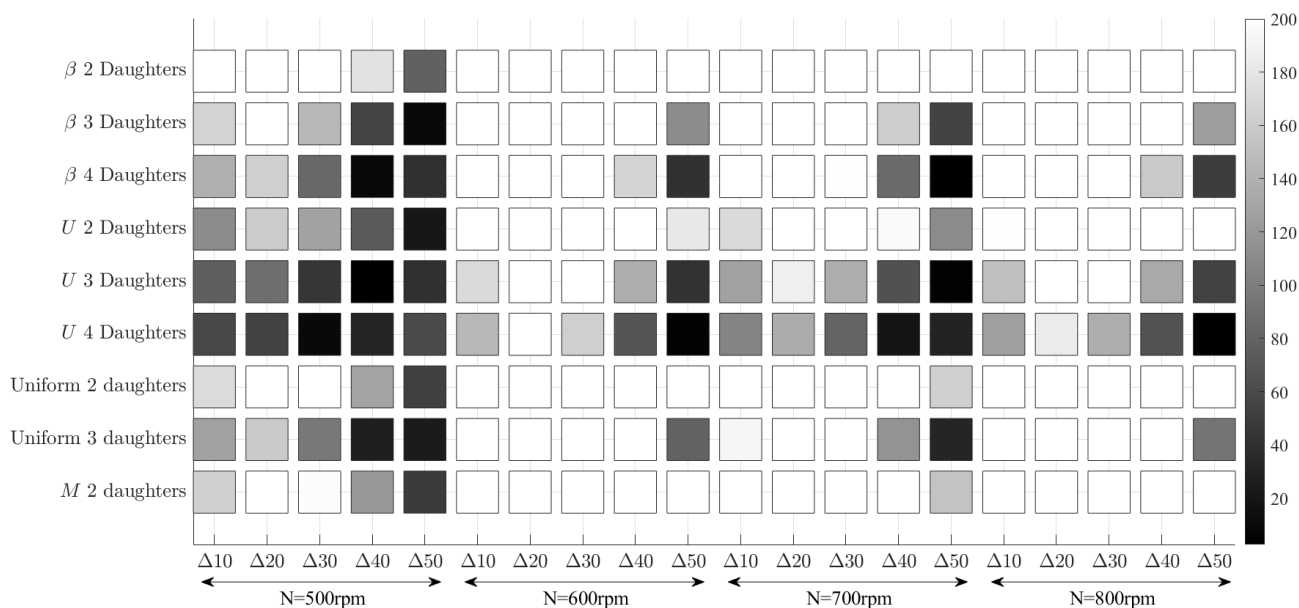


**Figure 3.** Numerical moment ratio percent deviation from the experimental values (Eq. (9)) for different DDFs and numbers of daughters in different operating conditions. White squares have deviations equal to or larger than 200 %.



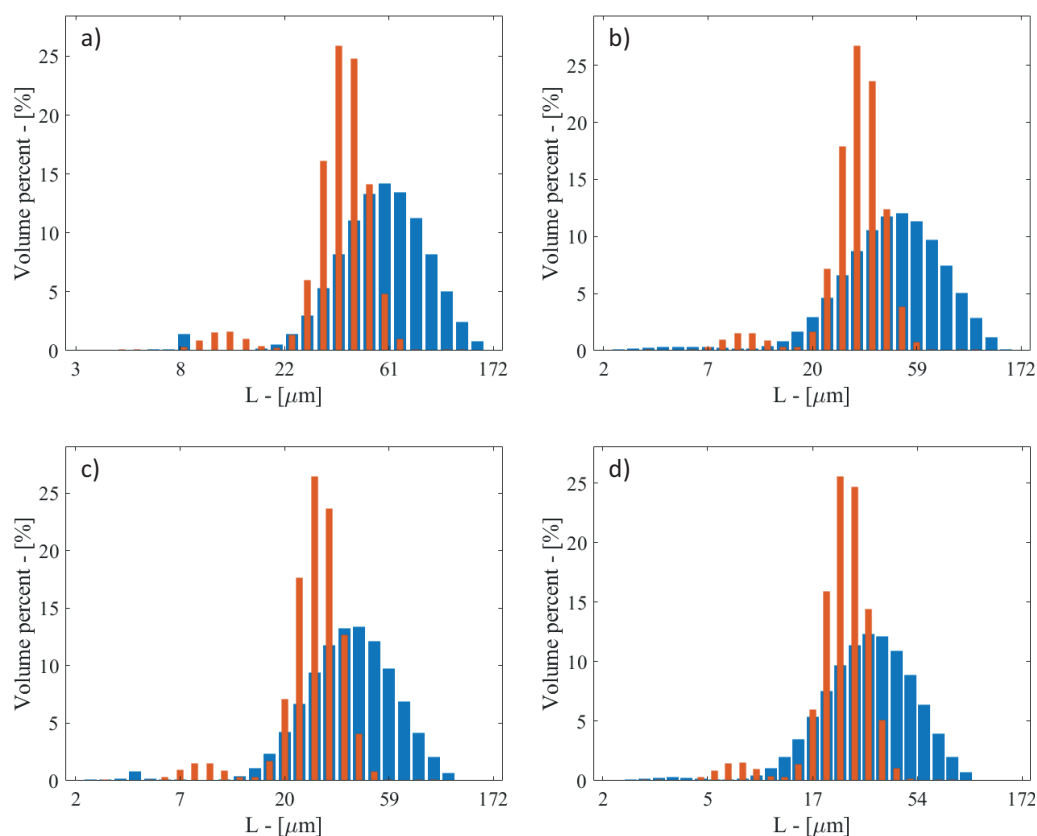


**Figure 4.** Experimental (in blue) and numerical (in red) DSDs, obtained with the U-shaped DDF producing four droplets for impeller rotational speeds equal to (a) 500 rpm, (b) 600 rpm, (c) 700 rpm, and (d) 800 rpm.

DSDs as predicted by the bell-shaped, U-shaped, uniform and M-shaped DDF with two daughters are shown, in terms of volume density functions.

Fig. 5 shows that the highest peak of the DSD is consistently predicted in all the simulations, and, for all the DDFs, it is located at a diameter of about  $47\text{--}30\text{ }\mu\text{m}$ , depending on the impeller rotational speed, with deviations between 16.2 and 17.9% from the experimental DSD, depending on the operating conditions and the DDF adopted. The largest differences are observable in the position of the second peak, which also changes the overall dispersion of the DSD. The bell-shaped DDF predicts two peaks that are close to each other, while the peaks predicted by the U-shaped DDF are separate. The position of the second peak predicted by the uniform and M-shaped DDFs is very similar and it lies in between the positions of the second peaks predicted by the beta and U-shaped DDFs.

Increasing the number of daughter droplets produced by a breakage event shifts the distributions towards smaller diameters, but it does not alter the shape of the final DSD, as shown in Fig. 6.

By means of example, Fig. 6 shows the DSD obtained by changing the number of produced fragments at the impeller rotational speed of 800 rpm. The behavior is similar in the other operating conditions and for different DDFs, which are not shown for brevity. Besides the noticeable shift produced by

a different number of fragments, increasing this number also increases the relative importance of the lowest peak, and this may contribute to explain why increasing  $p$  leads to a better agreement with the experimental moment ratio, as observed in Fig. 3.

## 5 Conclusions

In this study, the effect of the DDF on the resulting DSD was explored, it was shown that different DDFs change the shape of the final DSD, and the effect of the number of daughters produced by a breakage event was presented.

In this work, the experimental distributions are obtained from the analysis of a sample withdrawn from a stirred tank rather than reconstructing them from multiple measurements of single droplets breaking in controlled environments, and the shape of the resulting DSD can be better described with a U-shaped DDF with four fragments, which is consistent with the outcome of single-droplet breakage experiments [8, 12, 13].

The DDFs studied in this work did not allow obtaining complete agreement with the experimental DSD in the different operating conditions. To reach a better agreement between simulations and experiments, a comprehensive analysis would need to investigate different breakup and coalescence kernels, but this is outside the goal of this work.

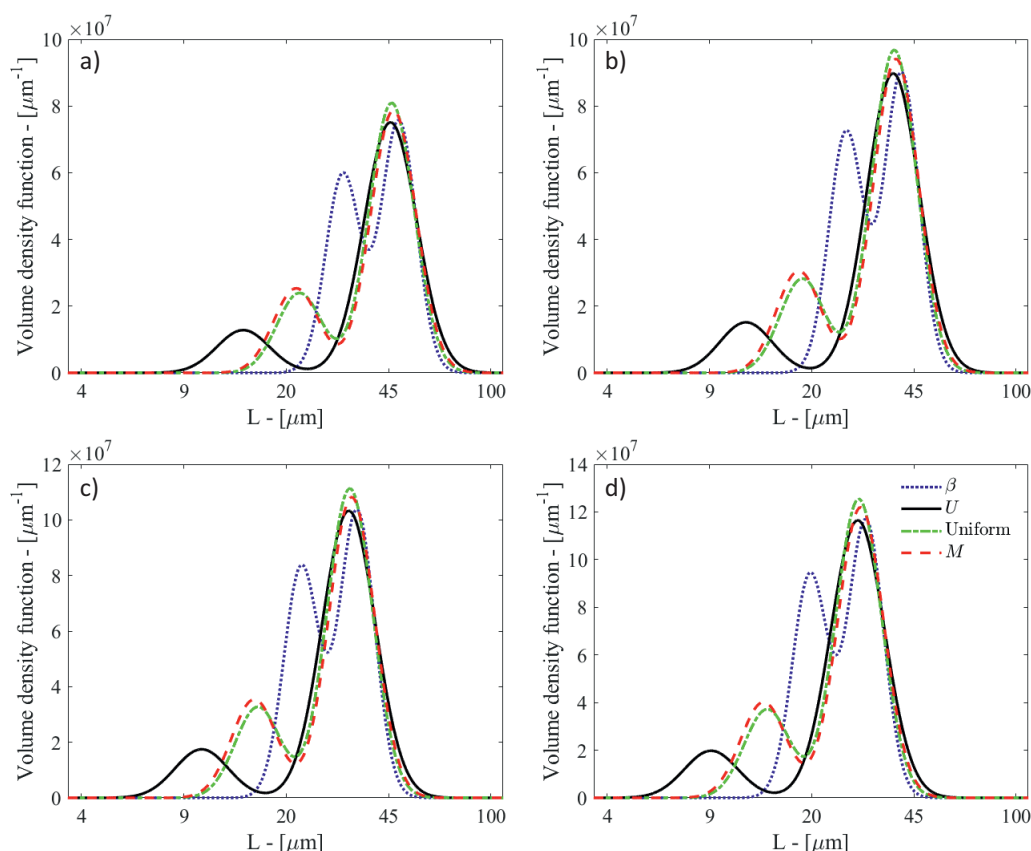


**Figure 5.** Numerical volume density function, obtained with different DDFs producing two droplets, for impeller rotational speeds equal to (a) 500 rpm, (b) 600 rpm, (c) 700 rpm, and (d) 800 rpm.

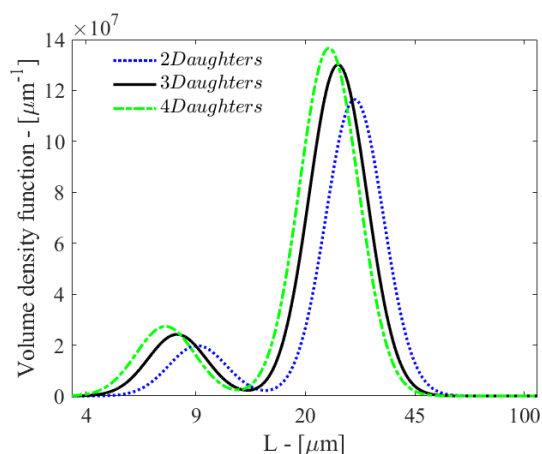


**Figure 6.** Numerical volume density function obtained at 800 rpm with the U-shaped DDF producing different numbers of daughter droplets.

## Data Availability Statement

Data available on request from the authors.

## Acknowledgment

Open Access Funding provided by Universita di Bologna within the CRUI-CARE Agreement.

*The authors have declared no conflict of interest.*

## Symbols used

$C_1^0$	$[m^{-2/3}]$	grid-independent parameter of the breakup kernel
$C_2^0$	$[-]$	grid-independent parameter of the breakup kernel
$C_3^0$	$[-]$	grid-independent parameter of the breakup kernel
$C_4$	$[-]$	daughter distribution function parameter
$F$	$[-]$	grid-dependent scalar correction of the breakup kernel
$g(\varepsilon)$	$[s^3 m^{-2}]$	turbulent dissipation rate
$h$	$[s^{-1}]$	breakup frequency
$\Delta k_0$	$[-]$	numerical moment ratio percent deviation from the experimental moment ratio



$L$	[ $\mu\text{m}$ ]	droplet diameter
$M_{k,0}$	[–]	ratio between the $k$ -th and 0-th orders moment
$n$	[ $\text{m}^{-3}$ ]	drop size distribution number density function
$N$	[rpm]	impeller rotational speed
$p$	[–]	number of fragments
$q$	[–]	daughter distribution function parameter
$r$	[–]	daughter distribution function parameter
$t$	[s]	time
$T$	[m]	tank diameter
$V$	[ $\text{m}^3$ ]	tank volume
$v(\epsilon)$	[ $\text{m}^3$ ]	volume of a computational cell

## Greek letters

$\beta$	[–]	daughter distribution function
$\epsilon$	[ $\text{m}^2\text{s}^{-3}$ ]	turbulent dissipation rate
$\mu$	[Pa s]	viscosity
$\rho$	[ $\text{kg m}^{-3}$ ]	density
$\sigma$	[ $\text{N m}^{-1}$ ]	interfacial tension

## Sub- and superscripts

C	continuous phase
D	dispersed phase
Exp	experimental
i	daughter droplet
j	mother droplet
k	moment order
Num	numerical

## Abbreviations

CFD	computational fluid dynamics
DDF	daughter distribution function
DSD	drop size distribution
EQMOM	extended quadrature method of moments
PBE	population balance equation
QMOM	quadrature method of moments
RANS	Reynolds-averaged Navier-Stokes

## References

- [1] D. L. Marchisio, R. O. Fox, *Computational Models for Poly-disperse Particulate and Multiphase Systems*, Cambridge University Press, Cambridge **2013**.
- [2] S. Castellano, L. Carrillo, N. Sheibat-Othman, D. Marchisio, A. Buffo, S. Charton, *Chem. Eng. J.* **2019**, 374, 1420–1432. DOI: <https://doi.org/10.1016/j.ces.2019.06.032>
- [3] M. Shiea, A. Buffo, M. Vanni, D. Marchisio, *Annu. Rev. Chem. Biomol. Eng.* **2020**, 11, 339–366. DOI: <https://doi.org/10.1146/annurev-chembioeng-092319-075814>
- [4] S. Falzone, A. Buffo, M. Vanni, D. L. Marchisio, *Adv. Chem. Eng.* **2018**, 52, 125–188. DOI: <https://doi.org/10.1016/bs.ache.2018.01.002>
- [5] E. H. Herø, N. La Forgia, J. Solsvik, H. A. Jakobsen, *Chem. Eng. Sci.* **2020**, 8, 100082. DOI: <https://doi.org/10.1016/j.ces.2020.100082>
- [6] Y. Liao, D. Lucas, *Chem. Eng. Sci.* **2010**, 65, 2851–2864. DOI: <https://doi.org/10.1016/j.ces.2010.02.020>
- [7] Y. Liao, D. Lucas, *Chem. Eng. Sci.* **2009**, 64, 3389–3406. DOI: <https://doi.org/10.1016/j.ces.2009.04.026>
- [8] R. Andersson, B. Andersson, *AIChE J.* **2006**, 52, 2020–2030. DOI: <https://doi.org/10.1002/aic.10831>
- [9] Y. Chen, J. Ding, P. Weng, X. Yang, W. Wu, *Chem. Eng. J.* **2020**, 386, 121826. DOI: <https://doi.org/10.1016/j.ces.2019.05.187>
- [10] B. O. Hasan, *Chin. J. Chem. Eng.* **2017**, 25, 698–711. DOI: <https://doi.org/10.1016/j.cjche.2017.03.008>
- [11] J. Solsvik, H. A. Jakobsen, *Chem. Eng. Sci.* **2015**, 131, 219–234. DOI: <https://doi.org/10.1016/j.ces.2015.03.059>
- [12] A. Zacccone, A. Gäbler, S. Maaß, D. Marchisio, M. Kraume, *Chem. Eng. Sci.* **2007**, 62, 6297–6307. DOI: <https://doi.org/10.1016/j.ces.2007.07.026>
- [13] H. Zhou, X. Yu, S. Jing, H. Zhou, W. Lan, S. Li, *Chem. Eng. Sci.* **2019**, 195, 23–38. DOI: <https://doi.org/10.1016/j.ces.2018.11.035>
- [14] V. Alopaeus, J. Koskinen, K. I. Keskinen, J. Majander, *Chem. Eng. Sci.* **2002**, 57, 1815–1825. DOI: [https://doi.org/10.1016/S0009-2509\(02\)00067-2](https://doi.org/10.1016/S0009-2509(02)00067-2)
- [15] H. Luo, H. F. Svendsen, *AIChE J.* **1996**, 42, 1225–1233. DOI: <https://doi.org/10.1002/aic.690420505>
- [16] F. Lehr, M. Millies, D. Mewes, *AIChE J.* **2002**, 48, 2426–2443. DOI: <https://doi.org/10.1002/aic.690481103>
- [17] F. Maluta, G. Montante, A. Paglianti, *Chem. Eng. Sci.* **2020**, 227, 115898. DOI: <https://doi.org/10.1016/j.ces.2020.115898>
- [18] F. Maluta, A. Buffo, D. Marchisio, G. Montante, A. Paglianti, M. Vanni, *Int. J. Multiphase Flow* **2021**, 136, 103547. DOI: <https://doi.org/10.1016/j.ijmultiphaseflow.2020.103547>
- [19] A. Buffo, J. De Bona, M. Vanni, D. L. Marchisio, *Chem. Eng. Sci.* **2016**, 153, 382–393. DOI: <https://doi.org/10.1016/j.ces.2016.07.032>
- [20] C. Y. Wang, R. V. Calabrese, *AIChE J.* **1986**, 32, 667–676.
- [21] M. Laakkonen, V. Alopaeus, J. Aittamaa, *Chem. Eng. Sci.* **2006**, 61, 218–228. DOI: <https://doi.org/10.1016/j.ces.2004.11.066>
- [22] R. B. Diemer, J. H. Olson, *Chem. Eng. Sci.* **2002**, 57, 4187–4198. DOI: [https://doi.org/10.1016/S0009-2509\(02\)00366-4](https://doi.org/10.1016/S0009-2509(02)00366-4)
- [23] P. J. Hill, K. M. Ng, *AIChE J.* **1995**, 41, 1204–1216. DOI: <https://doi.org/10.1002/aic.690410516>
- [24] D. Li, D. Marchisio, C. Hasse, D. Lucas, *Comput. Phys. Commun.* **2020**, 250, 107036. DOI: <https://doi.org/10.1016/j.cpc.2019.107036>
- [25] D. Li, Z. Li, Z. Gao, *Chin. J. Chem. Eng.* **2018**, 26, 2009–2013. DOI: <https://doi.org/10.1016/j.cjche.2018.04.032>
- [26] D. Li, Z. Gao, A. Buffo, W. Podgorska, D. Marchisio, *AIChE J.* **2017**, 63, 2293–2311. DOI: <https://doi.org/10.1002/aic.15557>